The molecular picture of the local environment in a stable model coacervate

Check for updates

Atanu Baksi[1], Hasan Zerze[1], Aman Agrawal[1,2], Alamgir Karim [1] & Gül H. Zerze[1] ✉

Complex coacervates play essential roles in various biological processes and applications. Although substantial progress has been made in understanding the molecular interactions driving complex coacervation, the mechanisms stabilizing coacervates against coalescence remain experimentally challenging and not fully elucidated. We recently showed that polydiallyldimethylammonium chloride (PDDA) and adenosine triphosphate (ATP) coacervates stabilize upon their transfer to deionized (DI) water. Here, we perform molecular dynamics simulations of PDDA-ATP coacervates in supernatant and DI water, to understand the ion dynamics and structure within stable coacervates. We found that transferring the coacervates to DI water results in an immediate ejection of a significant fraction of small ions (Na^+ and Cl^-) from the surface of the coacervates to DI water. We also observed a notable reduction in the mobility of these counterions in coacervates when in DI water, both in the cluster-forming and slab simulations, together with a lowered displacement of PDDA and ATP. These results suggest that the initial ejection of the ions from the coacervates in DI water may induce an interfacial skin layer formation, inhibiting further mobility of ions in the skin layer.

Solutions of two oppositely charged macromolecules often separate into two liquid-like phases with different viscosities, commonly referred to as coacervation/condensation, initially described by Bunderberg de Jong and Kruyt for colloidal mixtures[1] while the history of biomolecular condensates dates back nearly a century earlier[2–4]. Polyelectrolyte complex coacervates (PECCs) play crucial roles in biological contexts, e.g., intracellular organization[5–12] and prebiotic evolution[6,13,14]. Additionally, numerous applications of PECCs including their usage in food science applications[15,16] biomimetic adhesives[17–19], and emulsion stabilizers[20,21] spurred a growing interest in polyelectrolyte coacervates. Peptide-based coacervates have novel therapeutic applications, such as tissue regeneration and drug delivery systems[22]. Furthermore, efforts have been made to design controllable biomimetic field-responsive soft particles in the form of coacervates, which could serve as vehicles for transporting various reactive species related to synthetic drugs or genetic materials[23].

As these versatile coacervates are adapted for many promising applications, understanding the interactions that stabilize coacervates and drive their formation has become crucial. Accordingly, in addition to the efforts in advancing applications of PECCs, an appreciable amount of effort has been dedicated to studying their fundamental biophysical properties experimentally[24–35], shedding light on their thermodynamic stability, phase coexistence behavior, rheological properties, molecular partitioning. Moreover, theoretical[36–44] and computational[45–50] studies focused on determining molecular determinants of complex coacervation and

phase behavior of coacervates, predicting interfacial tension of coacervates, and explaining different thermodynamic contributors in coacervation process.

More recent efforts have aimed at producing thermally and chemically stable coacervates[23,51–53]. In earlier work, Williams et al.[51] reported that high ionic strength of solutions discourages the PDDA-ATP coacervation, emphasizing the significance of charge interactions in droplet formation and stability. They found that the formed droplets spontaneously become neutral or positively charged depending on the molar PDDA monomer to ATP ratio. Later, Agrawal et al. experimentally produced coacervates that do not coalesce over time into a macrophase[23]. They achieved this stability against fusion by transferring coacervates to a deionized environment, which presumably stabilizes their otherwise highly diffuse interfaces. Despite this significant advancement in the stability of PECCs (without requiring additives or chemical reactions), the underlying molecular picture leading to this stability has remained not well understood.

Although the aforementioned computational and theoretical studies have been instrumental in delineating the phase equilibrium and rheological properties of coacervates, the large (typically prohibitively large) costs of explicit solvation and related system size requirements have limited molecular dynamics (MD) simulation studies to modeling polyelectrolytes in implicit solvents[54–59]. Consequently, a molecular picture of changes in the local solvation environment (including explicit water and ions), dynamics, and structure stabilizing the complex coacervates have remained crucially

[1]William A. Brookshire Department of Chemical and Biomolecular Engineering, University of Houston, Houston, TX, 77204, USA. [2]Present address: Department of Chemistry and Pritzker School of Molecular Engineering, University of Chicago, Chicago, IL, 60637, USA. ✉e-mail: gzerze@uh.edu

needed, as it would allow the development of novel tools to control and tune the stability and properties of PECCs.

In this study, we aimed to understand the effect of local ionic solution environments on stable coacervates at a molecular level with the explicit presence of water and ions. To achieve this, we employed explicit-solvent coarse-grained (CG) MD simulations to study coacervates of polycationic polydiallyldimethylammonium chloride (PDDA) and anionic adenosine triphosphate (ATP) molecules in explicit water and counterions. CG models are widely used in molecular modeling to balance computational efficiency with sufficient accuracy for capturing the essential physical behaviors of large biomolecular systems. We chose the MARTINI model in particular, for its robustness and versatility in simulating complex biomolecular systems, including proteins, lipids, and nucleic acids. It offers a well-established parameter set that has been extensively validated against experimental data[60–64]. The CG definitions of PDDA monomer and ATP molecule are provided in Fig. 1A following earlier studies[65,66]. After equilibration and production simulations in the supernatant, the ionic environment was altered to deionized (DI) water (which is analogous to transferring the coacervates into DI water as in the experimental study[23]) to investigate the impact of this deionized environment on the coacervate structure and ion dynamics. A schematic description of the DI water transfer of coacervates is presented in Fig. 1B. We found that the PDDA-ATP coacervates remained positively charged in DI water. Importantly, we also found that a significant fraction of the small ions (Na^+ and Cl^-) within the coacervates are immediately ejected into the ion-deprived bulk solution when the coacervates are transferred to DI water with a subsequent slowdown in the ion dynamics for the ions remaining in the coacervates. The majority of the ejected ions used to reside on the surface of the coacervates before their transfer to the DI water. These findings led us to conclude that the initial ejection of the ions (most of which are ejected from the surface) contributes to the formation of an interfacial layer on coacervates in DI water, which is further evidenced by our measurement of the subsequent slowdown of ions. Additional slab simulations also showed an increased number of contacts between PDDA and ATP and a lowered PDDA and ATP displacement after the ion ejection
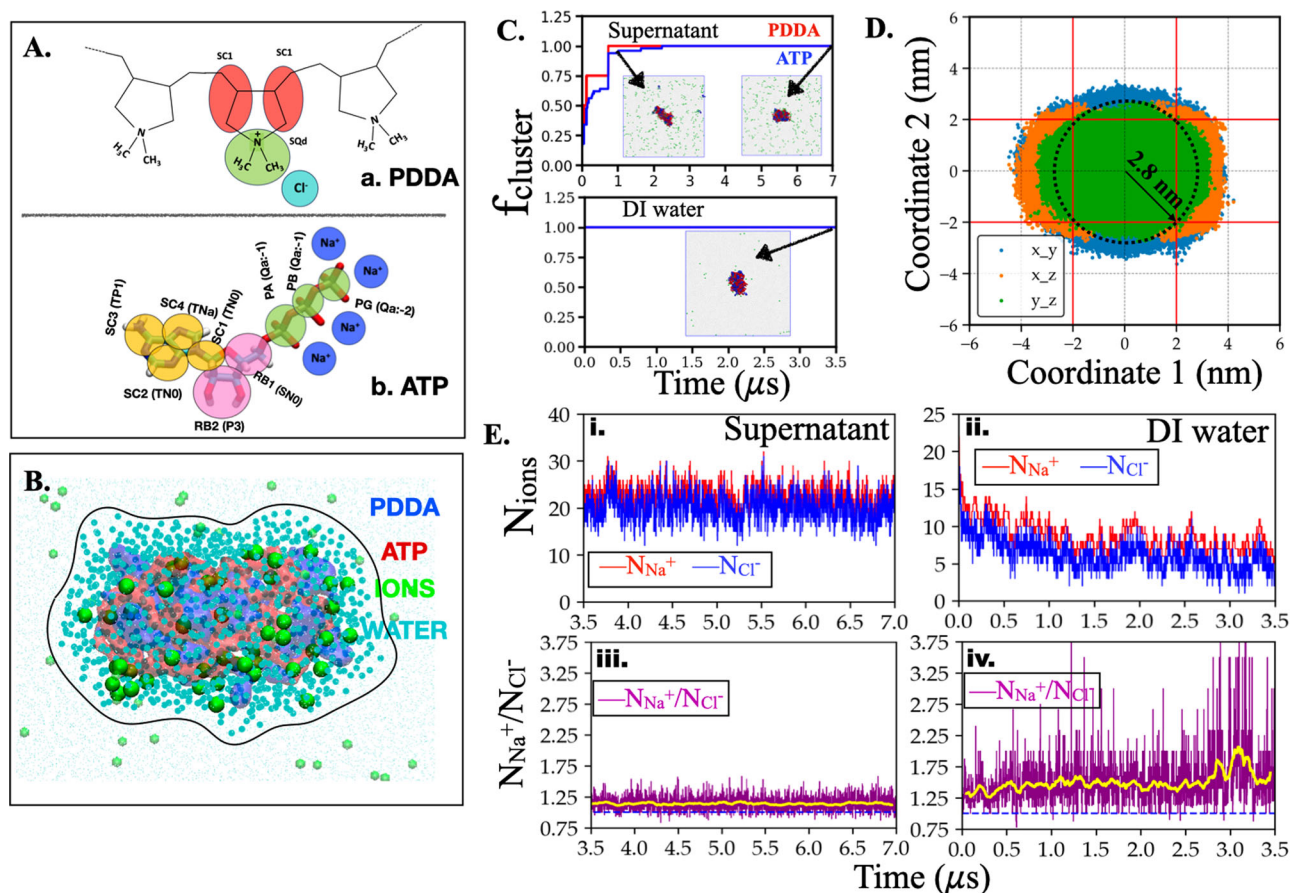

Fig. 1 | System definition, coacervate formation, and ionic nature of the coacervates. A Schematic representation of atomistic-to-coarse-grained (CG) mapping of PDDA monomer, ATP molecule implemented in this work. B A snapshot of PDDA-ATP coacervate with associated ions and water beads just before transferring it to DI water. Counterions and water molecules enclosed in the black curved boundary (a curved surface in 3D) are at a distance smaller than 1 nm to any PDDA or ATP beads. Counterions and water outside this surface are discarded while transferring. C Time evolution of the fraction of PDDA and ATP molecules in the largest cluster ($f_{cluster}$) in the supernatant (top) and DI water (bottom) for a selected simulation set. The same for all 8 sets are shown in Supplementary Figs. 18 and 19, respectively, for supernatant and DI water. We consider the cluster fully formed after $f_{cluster}$ reaches a stable value of 1.0. The snapshots in the insets are the simulation box at indicated simulation times where PDDA, ATP, and small ions beads are colored red, blue, and green, respectively. D Projection of the clustered PDDA and ATP beads' (coacervates) positions on three principal planes of the cluster for a selected set. The same for all 8 sets is shown in Supplementary Fig. 20. This projection informs about the coacervate size and shape (e.g., asphericity). We also used these projections to label the "surface" and "core" of coacervates. The overlapping rectangular area is used to identify a core represented by a sphere with a radius of $r_{core} = 2.8$ nm. In between $r_{core} = 2.8$ nm and $r_{surface} = 5$ nm is considered as surface. Here, coordinate 1 and 2 are the pairs of principal axes orthogonal to the projected axis. Three colored regions are projections of PDDA and ATP beads on three principal planes. E Time evolution of the number of Na^+ and Cl^- ions within the coacervate in "supernatant" after the coacervate forms (i) and "DI water" (ii) for a selected set. Time evolution of the ratio of the number of Na^+ to Cl^- ions within the coacervate in "supernatant" (iii) and "DI water" (iv) for a selected set. The same for all 8 sets are shown in Supplementary Figs. 1 and 2, respectively, for supernatant and DI water. Yellow lines in the lower panel indicate a running average (which is higher than 1) both in supernatant and DI water.

supporting this conclusion. Agrawal et al.[23] have originally hypothesized the interfacial skin layer formation in DI water; this work provides direct quantification of electrostatic changes upon DI water transfer, lending further support to the skin layer formation hypothesis with direct evidence and marks the first extensive investigation of molecular picture of the electrostatic changes in such stable coacervates.

Results and discussions

We produced and analyzed an aggregated sum of 63 μs simulation data of PDDA-ATP coacervates in explicit water and ions when they are in supernatant and deionized (DI) water. Formation of the coacervate from the dispersed PDDA and ATP molecules in an aqueous medium can be discernable through the time evolution of PDDA and ATP fraction in the cluster, as shown in Fig. 1C. To analyze the region-specific ion dynamics, we defined the regions in the coacervates projecting PDDA and ATP positions on three principal planes; an example of which is shown in Fig. 1D for a selected coacervate. More details about the time evolution of PDDA and ATP fraction in the largest cluster and the protocol for defining regions namely "surface" and "core" of coacervates have been provided in the "Methods" section.

Ionic nature of the cluster

We first quantified the ion distribution in coacervates both in ionic supernatant and in DI water (i.e., after transferring the coacervates to DI water). We counted the number of Na^+ and Cl^- ions within the coacervates. Since all of our PDDA and ATP molecules are clustered in the coacervates (i.e., no PDDA or ATP in the bulk solution), the ions that are at a distance smaller than 1 nm to the PDDA and ATP beads are considered to be in the coacervates. Figure 1E depicts the time evolution of ion numbers within the cluster (upper panel) and the ratio of the positive (Na^+) to negative (Cl^-) ions (lower panel) in the supernatant (i, iii) and DI water (ii, iv) for a selected simulation. The ratio is consistently observed to be greater than 1.0 in both "supernatant" and "DI water" for all the independent simulations (Supplementary Figs. 1 and 2, respectively). Given that PDDA and ATP molecules have equal and opposite charges and are always clustered within the coacervates (i.e., no PDDA or ATP in bulk solution), the Na^+/Cl^- ratio being larger than 1 means the coacervates are positively charged.

We have observed that the number of Na^+ and Cl^- ions within the coacervates initially decreases as a function of simulation time after the coacervate was transferred to DI water as seen in Fig. 1E(ii) while Na^+ to Cl^- ratio increases (Fig. 1E lower panels' comparison, and Supplementary Figs. 1 and 2 panels' comparison). The former is a result of the concentration gradient of ions that favors the movement of ions towards the initially ion-free bulk phase. We note that the number of Na^+ and Cl^- ions maintain equilibrium after 1.5 μs. We found that the Na^+ to Cl^- number ratio, slightly increases almost immediately, after placing the coacervate into DI water (see Fig. 1E(iv)).

Density profile and size of the cluster

We also analyzed the density of the PDDA, ATP, counterions, and water molecules within the coacervates (Fig. 2A). PDDA and ATP density profiles showed that the PDDA-ATP clusters both in the supernatant and DI water extend up to a radius of about 5 nm from the center of the cluster (Fig. 2A i., ii.). As a guide to the eye, we indicated this 5 nm radius with vertical dashed lines in Fig. 2A but we note that this vertical line does not necessarily define the surface boundary of the coacervates due to the deviations from a spherical shape at this length scale as discussed below (last paragraph of this subsection and the first paragraph of *Ion dynamics within coacervates* subsection).

We found that the coacervates contain a significant amount of water and ions after transferring them to DI water in agreement with their liquid-like nature. We note that the water density plateaus at around 862 kg/m³, which is consistent with the bulk density of this water model at these thermodynamic conditions (Supplementary Fig. 3). Since our cluster size is relatively small, PDDA and ATP densities inside the coacervate do not have

a clear plateau, however, the data were sufficient to produce sigmoidal fits (Supplementary Fig. 4). From the sigmoidal fits, we predict the average PDDA and ATP densities in the coacervates (C_{dense}) as approximately 540 kg/m³ and 536 kg/m³, respectively, in the supernatant. In DI water, C_{dense} for PDDA is approximately 511 kg/m³ and that for ATP is approximately 566 kg/m³ (Supplementary Fig. 4). In addition, we estimated the average water content (mass fraction) within the coacervates by calculating the total mass of water molecules present within the core region of the coacervate (water molecules that are at a distance of 2.8 nm to the center of the coacervate) and normalizing it with the total mass of the molecules (PDDA, ATP, ions, and water) within the core. We found that the average water content within the coacervate core is approximately 43% and 40% in the supernatant and DI water systems, which is smaller than the experimental measurements of 70% and 65% (by mass) of water in the supernatant and DI water, respectively[23]. We found even smaller water content within coacervates in slab simulations (see Fig. 3A for the density profiles of water, PDDA, ATP, and small ions and B for snapshots from the slab simulations). The fraction of water at the center of the slab is estimated to be about 10% and 13% for supernatant and DI water conditions.

We found that the mass density profiles of PDDA and ATP within the coacervates are similar to each other, for both supernatant and DI water systems, with slightly larger ATP concentrations at the center for both systems (Fig. 2A, top panels). Note that this slight difference in concentration is amplified by the four-fold difference in ATP ($-4e$) and PDDA monomer ($+1e$) valence, making the core of the coacervates more negatively charged. We also visually detected that ATP occupies a larger portion of the center (Supplementary Movie 1), which becomes more pronounced after transferring the coacervates to DI water. We also found that Cl^- ions mostly occupy the surface of the coacervates whereas the Na^+ ions populate more evenly at the center of the supernatant coacervates (Fig. 2A, bottom panels). The slightly larger concentration of ATP at the coacervate center is consistent with the larger Na^+ concentration at the center.

Salt and counterion partitioning in coacervates have been studied experimentally[67], computationally[41], and theoretically[68]. Experimentally obtained phase diagrams of coacervates of oppositely charged polypeptides showed larger salt concentrations in the dilute phase[67]. This finding was consistent with calculations from PRISM theory[41], which predicts larger salt concentration in the dilute phase under typical conditions modeled in their work. Contrary to these findings, we found higher Na^+ and Cl^- concentrations in our clusters (Fig. 2A iii.). However, this observation is the opposite in our slab simulations. Figure 3A iii. shows a lower counterion concentration in the slab (compared to the dilute phase). We argue that this difference in counterion partitioning is a result of the difference in total ionic concentration. Our slab simulations have a significantly larger ionic concentration (920 mM without added salt) than the cluster-forming simulations (20 mM). Recent theoretical observations showed a difference in salt partitioning similar to our findings: the coacervate has a higher salt fraction at low total salt concentrations whereas the dilute phase has a higher salt fraction at high salt concentrations[68].

While the macroion density profiles remain similar, two important changes happen to the counterion density profiles upon transferring the coacervates to DI water. (1) Ion densities in the coacervates drastically drop after they are placed in DI water. The majority of the ions from the coacervates are ejected into the bulk solution after being placed in DI water (Fig. 1E ii., also see Supplementary Movie 1). (2) Na^+ ion density peaks more sharply at the center after DI water placement (Fig. 2A iii., iv.). In both supernatant and DI water, the core region of the coacervates is populated more by Na^+ ions and the difference between Na^+ and Cl^- density profiles becomes more pronounced after DI water placement. Na^+ ion density profile sharply peaks at the center with a monotonic decrease as the distance away from the center increases in DI water while the Cl^- density trend remains similar in DI water to that in supernatant. The Na^+ ions being buried at the center of the coacervates significantly affects the ion dynamics within the coacervates, which we quantified in *Ions dynamics within coacervates* subsection.
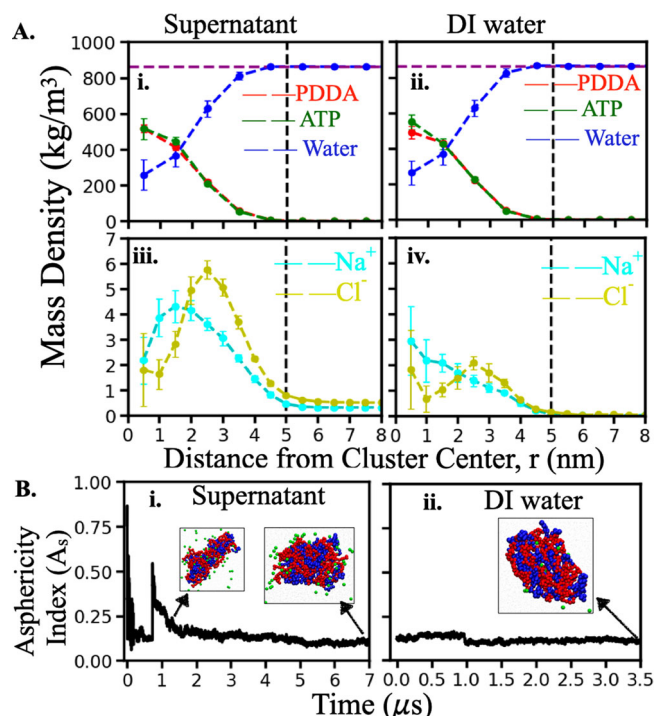
Fig. 2 | Density profiles and asphericity of the coacervates. A Mass density profiles of PDDA, ATP, water, and ions in supernatant (left panels) and DI water (right panels). Error bars are the standard deviation of sample means. The density profiles are averaged over eight independent simulations. The vertical line at 5 nm is the guiding line indicating the maximum extent of the cluster. The horizontal line at 862 kg/m³ refers to equilibrated MARTINI 2.0 water density at 298 K. The molecular weight of each PDDA monomer in its fully dissociated state is 126.21 g/mol and that of an ATP molecule at the protonation state of $-4e$ is 503.2 g/mol. The molecular weight of water, Na^+ and Cl^- ions are 18.01, 22.99, and 35.45 g/mol, respectively. **B** Time evolution of asphericity index of the largest cluster in (i) supernatant (ii) DI water for a selected run. The same for all eight sets are shown in Supplementary Figs. 5 and 6 for supernatant and DI water, respectively. The relative (relative to mean) standard deviation in the last 2 microseconds simulation data averaged over all (8) sets is found to be 10.8% and 7.6% in supernatant and DI water, respectively. Attached snapshots in the inset are the clusters at indicated simulation times where PDDA, ATP, and ion beads are colored in red, blue, and green, respectively.

Since the density profiles provide limited information about the shape of coacervates, we calculated the asphericity index, A_s, of the coacervates. Instantaneous A_s of coacervates is calculated following Eq. (1) (see the "Methods" section) as a function of time. Figure 2B shows the time evolution of A_s of the largest cluster for both (i) supernatant and (ii) DI water systems for one of the simulation sets with the snapshots of the coacervates collected at indicated simulation times. A_s and the representative snapshots of the coacervates for all independent simulations are presented in Supplementary Figs. 5 and 6 for supernatant and DI water systems, respectively. These results show that the asphericity index of the well-stable coacervates (after simulation time 3.5 μs) varies within $0.1 < A_s < 0.4$ for different independent simulations. We observe after transferring the clusters to DI water, coacervate morphology exhibits minimal variation, characterized by a low degree of fluctuation. This observation is consistent with the higher stability of the coacervates in DI water as compared to supernatant systems.

Ion dynamics within coacervates
To further extend our understanding of the coacervate stability in DI water, we analyzed the dynamics of the counterions within the coacervate surface and core, both in supernatant and in DI water. As our coacervates are not perfectly spherical (see the subsection above), we first identified the "core" and "surface" regions in our coacervates based on the principal axes
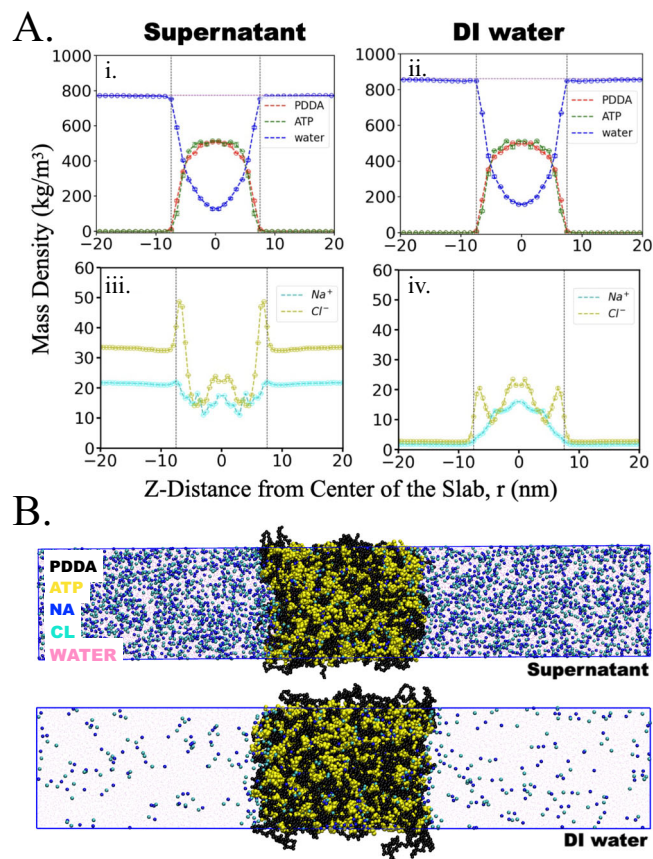

Fig. 3 | Density profiles and snapshots of slab simulations. A Density profiles of (i) PDDA, ATP, and water in the supernatant, (ii) PDDA, ATP, and water in DI water, (iii) Na^+, and Cl^- in the supernatant, and (iv) Na^+, and Cl^- in DI water. **B** Snapshot of the PDDA-ATP slab with counterions and water beads (transparent pink) in the supernatant (top) and DI water (bottom).

projection (Fig. 1B). For the full protocol of the principle axes projection and labeling, see the "Methods" section.

Time evolution of the location of tagged ions after transferring the coacervates to DI water. Following the definition of the "core" and "surface" regions, we tagged the Na^+ and Cl^- ions as initially-core and initially-surface ions at the time of transferring the coacervates to DI water. We then followed the displacement of tagged ions from their initially tagged region (surface or core) to other (surface, core, or bulk solvent) regions and calculated the fraction of initially tagged ions in those regions throughout the simulation time. Figure 4A shows the fluctuations as a function of time for one of the simulations, where the upper panel depicts the time evolution of the fraction of initially surface ions that stay on the surface (green) or move to bulk solvent (red) or core (black). Figure 4B represents the time evolution of the fraction of initially-core ions that stay in the core (black), and move to the surface (green) or to bulk solvent (red). We find the ions from the coacervates are rapidly ejected in the ion-deprived DI water solvent as can be seen in the bottom panels of Fig. 4A, B. A schematic diagram of the rapid ejection of these initially tagged ions is presented in Fig. 4C. We note that this rapid ejection is consistent with our experimental measurements of ionic conductivity[69]. Over time, we calculated that ~75% of the initially-surface ions move to the bulk region outside the cluster, and the remaining (~25%) ions remain inside the cluster (core or surface region). On the other hand, only ~60% of the initially-core ions are found to move to the bulk region and the remaining initially-core ions stay within the coacervate (in the core or the surface).
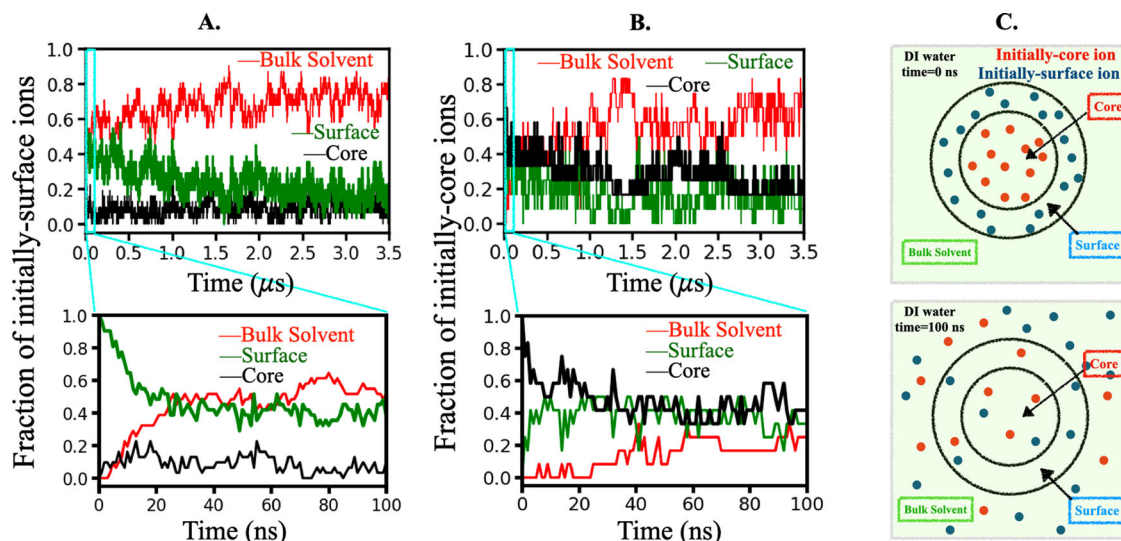
Fig. 4 | Signature of rapid ejection of ions from coacervates upon transferring them to DI water. The ions located within a spherical region of radius $r_{core} = 2.8$ nm are labeled as core ions whereas the ions located in the spherical region between $r_{core} = 2.8$ nm and $r_{surface} = 5$ nm labeled as surface ions at $t = 0$ ns. Results are shown for one simulation set. Results for other sets are shown in the Supplementary Fig. 20). Ion ejection from the surface (**A**) and from the core (**B**). The top panels in **A** and **B** show the time evolution of the label change of the ions initially labeled as "surface" and the time evolution of the label change of the ions initially labeled as "core", respectively, after coacervates transferred to DI water. The initial 100 ns of the simulation data is zoomed in on the bottom panels of **A** and **B** to show the initial rapid ejection both from the surface (**A**) and from the core (**B**). **C** Schematic diagram of the ejection of initially-core and initially-surface ions.

These findings indicate that a large percentage of both the initially-surface and initially-core ions transition to the bulk solution but significantly more of the initially-surface ions will transition to bulk solvent compared to initially-core ions. We observed a similar trend in all eight simulations in DI water (shown in Supplementary Figs. 7 and 8). We also calculated the contribution of core and surface regions towards total ions ejected in DI water. We found that on average ~65% of the ions ejected into DI water come from the coacervate surface whereas ~35% come from the coacervate core.

Interfacial skin layer formation in DI water. We argue that the PDDA and ATP molecules remaining after the ejection of small counterions crosslinks with each other to form a skin layer at the interface[23] in DI water. To provide support for this argument, we calculated the time-dependent mean squared displacement (MSD) of PDDA and ATP molecules in supernatant and DI water. Although the differences in MSD in cluster-forming simulations were insignificant, we conducted slab simulations and measured the MSD of PDDA molecules in both lateral and longitudinal directions for further insights into skin layer formation (Supplementary Fig. 21). We note that ions are rapidly ejected from the slab surface similar to clusters in cluster-forming simulations (Fig. 3A iii., iv.) and we measured the MSD after discarding at least 1 μs of the simulation data from the beginning. The MSD along the lateral directions (xy) indicated a lower PDDA and ATP diffusivity for the coacervates in DI water compared to those in the supernatant (Supplementary Fig. 21). This suggests that the macroions PDDA and ATP slow down in DI water and this slowdown is consistent with a skin layer formation, blocking the mobility of ions in the coacervate core. We note that the MSDs of PDDA (Supplementary Fig. S21A) and ATP (Supplementary Fig. S21B) are nearly identical since PDDA and ATP hold strongly onto each other and displace together in both the supernatant (Supplementary Movie 2) and DI water (Supplementary Movie 3).

To investigate the skin layer further, we analyzed whether macroions are structured in the coacervate core or surface. We calculated the average number of ATP-PDDA contacts (per ATP bead) in both the surface and core regions of the slab under supernatant and DI water environments (see Supplementary Tables 13 and 14). In the surface zone, DI water caused a small but noticeable increase in ATP-PDDA contacts, from 2.29 to 2.42, indicating denser surface packing and supporting the formation of an

interfacial skin layer. In the core zone, the average number of contacts remained nearly the same (2.91 to 2.87) within statistical limits.

Ion residence times depend on the location in the coacervate. How long do ions reside in a particular region (core or surface) before moving to a different region (core, surface, or bulk solvent)? To answer this question, we calculated the ion residence times, from a time correlation function, $C_{res}^{ion}(t)$, for the ions residing in the core and the surface regions, for both in the supernatant and DI water surroundings following Eq. (2), and Eq. (3) for cluster-forming simulations (see "Methods" section for details). The correlation function decays are presented in Supplementary Figs. 9–14. Furthermore, to qualitatively understand contributions from oppositely charged counterions on total ion dynamics, we also separately analyze the correlation decay of Na^+ and Cl^- ions, individually. Supplementary Figs. 9 (for supernatant) and 10 (for DI water) show the time-dependent decay of the residence time correlation function for all ions collectively (Na^+ and Cl^- ions combined); Supplementary Figs. 11 (for supernatant) and 12 (for DI water) show the same for positively charged Na^+ ions only; and Supplementary Figs. 13 (supernatant) and 14 (DI water) show the same for negatively charged Cl^- ions only. Timescales associated with these correlation decays are estimated using Eq. (4) mentioned in the "Methods" section. Fits are presented together with raw data on the plots from Supplementary Figs. 9–14.

We found that the correlation decays for all the ions residing in the "core" regions from all the independent simulations can be adequately described with three distinctive characteristic timescales, (1) of the order of nanoseconds, $\tau_{fast} < 10$ ns, (2) of the order of tens of nanoseconds (10 ns $< \tau_{intermediate} < 200$ ns), and (3) of the order of hundreds of nanoseconds to tens of microseconds (200 ns $< \tau_{long} < 50$ μs). On the other hand, for all ions residing in the "surface" region, the correlation decays exhibit mainly two characteristic timescales, which were previously identified as the first two timescales describing "core" ion dynamics, τ_{fast} and $\tau_{intermediate}$. The fast timescale (τ_{fast}) can be attributed to the rapid exchange of ions between different regions, whereas the intermediate timescale ($\tau_{intermediate}$) is associated with the translational motion of ions within those specific regions. The slowest characteristic timescales τ_{long} are indicative of kinetically trapped ions, compelling them to remain in the particular region for an extended duration.
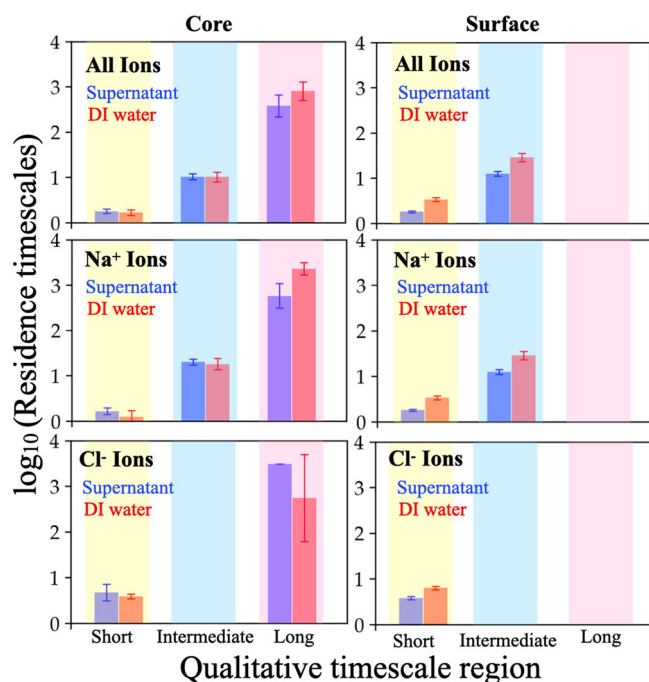
Fig. 5 | Comparison of characteristic timescales ($\log_{10}(\tau)$) describing ion residence correlation decays in "core" (left panel) and "surface" region (right panel). The top panels report the timescales associated with overall ion dynamics whereas the middle and bottom panels report the same separately for Na^+ ions and Cl^- ions, respectively. Each plot compares the dynamics of ions in the supernatant and DI water system.

Characteristic timescales observed from different independent simulations are summarized in Supplementary Tables 1–12. The timescales (with associated amplitude) that are averaged over all independent simulations and their standard deviations (as errors) are reported in Fig. 5 in log scale (The same for slab simulations reported in Supplementary Fig. S22). The left panels in Fig. 5 represent residence timescales of ions residing in the "core" region whereas the right panels depict the same for ions residing in the "surface" region. The top panels show the characteristic timescales describing correlation decays with contribution from all ions, whereas the middle and bottom panels show the same for only Na^+ ions and only Cl^- ions, respectively. The comparisons between the residence times in supernatant and DI water systems are provided in each panel.

The comparisons from Fig. 5 showed three interesting findings:

(1) The positively charged Na^+ ions are rate-limiting for ion dynamics, which is consistent with them being buried in the coacervate core. Negatively charged Cl^- ions are much shorter lived within the surface region and move relatively faster compared to their positive counterpart, Na^+ ions.
(2) Ions residing in the "surface" region are faster compared to ions that are residing in the "core" region. This has been observed systematically over all the independent simulations both in supernatant and DI water systems.
(3) Ions, particularly the rate-limiting Na^+ ions within the coacervates, exhibit longer lifetimes in DI water systems compared to those in supernatant systems.

Concluding remarks
Complex coacervates are highly attractive materials as drug delivery agents, protocellular environments, and model membraneless organelles. However, at thermodynamic equilibrium, small coacervate droplets coalesce to form a condensed macro phase limiting the range of their applications. Recent work by Agrawal et al.[23] showed that it is possible to stabilize coacervates against coalescence in a deionized environment, however, the underlying

molecular picture of this stability remained elusive and challenging to obtain experimentally.

How does changing the equilibrium environment of coacervate surroundings affect the dynamics of its components? Our findings show interesting ion dynamics when such a non-equilibrium change is introduced in the form of deprivation of counterions from the supernatant. Counterions within the coacervates were rapidly ejected into bulk solution upon DI water transfer. Importantly, the majority of those ejected ions were ejected from the coacervate surface. Subsequently, the ion residence times became at least an order of magnitude slower within coacervates and ionic density profiled underwent restructuring in DI water whereas the density distribution of PDDA, ATP, and water molecules within the coacervates remained mostly unchanged. Since we do not measure a significant change either in the water content or in the polymer density of the coacervates before and after DI water transfer, we do not have an obvious reason for a viscosity change in the coacervates. Since we eliminate the reasons for a viscosity change, we argue that our findings are consistent with skin layer formation (slowing down the ions inside coacervates), supporting the original hypothesis by Agrawal et al.[23].

We also consistently quantified that PDDA-ATP coacervates carry a net positive charge in the ionic supernatant throughout all our independent simulations. We argue that the characteristic charge of the coacervates and the slow counterion (i.e., Na^+ or Cl^-) is determined by the relative size of the macroions. We observed that the smaller macroion (ATP) often arranges itself as small clusters inside the coacervate (Supplementary Movie 1) and has a slight preference for the center, which becomes more pronounced upon transferring the coacervates to DI water. The slight increase in the ATP concentration in the center is accompanied by a larger concentration of the oppositely charged Na^+ counterion at the center, making Na^+ ions slower. We also performed the charge-personality swap simulations, that is, simulations of hypothetical PDDA-ATP systems where we swap the charges of PDDA and ATP molecules (i.e., PDDA beads were made negatively charged and ATP beads were made positively charged, keeping everything else the same, including identities of the counterions, bonded interactions, van der Waals interactions, etc.). We found that the Cl^- ions predominate the Na^+ ions in the coacervates in that case (Supplementary Fig. 15), making them negatively charged. Moreover, Cl^- becomes more buried in the coacervate core and becomes the slower counterion in that case (Supplementary Figs. 15 and 16). These findings support our argument that the characteristic charge depends on the relative size of the macroions. The counterion that is oppositely charged to the smaller macroion prefers to occupy the core, becomes the slow ion, and predominates the other counterion in number determining the net charge of the coacervate.

This work shows that the coacervates stabilized in DI water exhibit distinct changes to their ionic attributes such as the rapid ejection of small counterions, a subtle change in total net charge, and altered ion dynamics. We believe that these observations apply to systems with macroions of largely different sizes (e.g., $(PDDA)_{50}$ and ATP) as discussed above. This work marks the first investigation of the molecular picture of the local ionic environment of PECCs which are stable against coalescence, enabling further investigation to produce and understand stable PECCs with various macroion sizes and valence.

We also performed slab simulations (Fig. 3) with larger system sizes (50 PDDA polymers and 625 ATP molecules, 920 mM ionic concentration) to complement our findings, which provided additional insights into the skin layer formation such as denser surface packing and mean-square displacement analyses (results are primarily presented in the Supplementary Information). We note that further investigation is still needed to obtain a more complete picture. Despite the increased system size in the slab simulations, more extensive simulations are necessary for a comprehensive quantification of local structuring and polymer arrangements on the surface. Since these simulations are performed in explicit solvent, larger systems have high costs to sample all relevant parts of the phase space. Future investigations with advanced sampling techniques will provide more information about the local polymer conformation on the coacervate surface, giving us a more complete

picture of the forces stabilizing the coacervates against coalescence. Furthermore, extending this study to other polyelectrolyte complex coacervates, including those formed with different polymer sizes and compositions, could examine the generalizability of the findings from this study.

Methods

In this work, we performed explicit-water CG MD simulations of an aqueous solution of polycationic PDDA and ATP molecules in the explicit presence of counterions as in the experimental solutions[23]. We chose this model system to study polyelectrolyte coacervation phenomena because of the availability of experimental data[23,51], where the formation of well-stable coacervates/condensates have been studied in detail.

In order to ensure adequate statistical significance, proper uncertainty quantification, and reproducibility of our findings, we performed eight independent simulations starting from randomly monodispersed mixtures of PDDA and ATP. We calculated the standard deviation of the sample mean as an error estimate and presented them as error bars in plots whenever appropriate. We calculated the errors via the following expression, $\epsilon = \frac{\sigma_{std}}{\sqrt{N_{sample}}}$ where N_{sample} is 8 (both for supernatant and DI water) and σ_{std} is the standard deviation, calculated as $\sigma_{std} = \sqrt{\frac{\sum (x_i - \mu)^2}{N_{sample}}}$ where the sum runs over N_{sample}. x is the value of the corresponding observable for the given sample, and μ is the sample mean.

Modeling and force field

We modeled the PDDA[65] and ATP[66] molecules with MARTINI 2.0 CG model in explicit water and ions. We fixed the length of each PDDA molecule as 50 monomers and each monomer has a quaternary amine group with a permanent charge of $+e$, i.e., each PDDA molecule has a total charge of $+50e$. We adjusted the protonation state of a single ATP molecule as $-4e$, in accordance with its nearly complete dissociation behavior at pH 7[70]. The schematic CG representation implemented in this work has been provided in Fig. 1A. Our systems consist of 4 PDDA chains (50 monomers each) and 50 ATP molecules. This selection is made to attain charge matching between the positively and negatively charged polyelectrolytes and 20 mM ionic concentration (i.e., 20 mM PDDA monomer concentration and 5 mM ATP concentration) as examined in a recent experimental study[23]. We initialized our systems as randomly dispersed PDDA and ATP molecules within a cubical box of ~25 nm to achieve 20 mM ionic concentration. We also added 200 positively charged and 200 negatively charged small ion beads to mimic solution conditions (i.e., supernatant). For positively and negatively charged small ions, we used Na^+ and Cl^- ion beads, respectively. We solvated the box with non-polarizable MARTINI 2.0 water[71]. We refer to these simulations as the PECCs in concentrated "supernatant" conditions. We simulated each independent supernatant simulation (8 total) for at least 7 μs.

We also simulated deionized (DI) water conditions by transferring the coacervates formed in supernatant conditions to pure water. In order to initialize the DI water simulations, we first isolated the coacervates formed in supernatant conditions including the PDDA, ATP, water, and ion beads enclosed in the coacervates. We described the coacervate identification protocol in the "Cluster analysis" subsection. We included all the ions and water beads at a distance smaller than 1 nm to any PDDA or ATP beads and then solvated these coacervates in pure water. We referred to the simulations as the PECCs in "DI water" conditions. See Fig. 1B for a visual representation of a transferred coacervate. For each supernatant system, we have one corresponding DI water system. We refer to a given pair of supernatant and corresponding DI water system as one "set", so we have a total of 8 sets. We started each independent DI water simulation (8 total) from the preformed coacervate of their corresponding supernatant simulations (as in the last saved snapshot of the corresponding supernatant system). We then simulated each independent DI water simulation (8 total) for 3.5 μs. We analyzed all supernatant and DI water simulations over the last 3.5 μs trajectories. Both for the supernatant and DI water system, we modeled 10% of the water beads as antifreeze type[71] to prevent freezing of the MARTINI 2.0 CG water.

We note that the PDDA force field parameters used in this work were originally developed for PDDA30 chains[65] solvated in polarizable MARTINI water[72]. In order to justify the compatibility of PDDA parameters with the non-polarizable water, we carried out simulations of PDDA30 solvated in the non-polarizable MARTINI 2.0 water model and compared pair correlation function and monomer-to-monomer distance distribution with the PDDA30 in polarizable water along with all-atom simulations as performed by Vogele et al.[65]. These comparisons are shown in Supplementary Fig. 17. Although we observe PDDA30 to be more compact when solvated in the LJ water compared to that when solvated in the polarizable water, their structural properties such as radial distribution function and distribution of monomer-to-monomer distances remained qualitatively the same, lending confidence in using the force field combination that we used in this work.

Slab simulation methodology.

A slab system was constructed starting with 50 pre-equilibrated poly(diallyldimethylammonium) (PDDA) chains and 625 adenosine triphosphate (ATP) molecules. These components were initially dispersed randomly within a periodic simulation cubic box. The dimensions of this box were set to $L_x = L_y = L_z = 9.5$ nm. The system underwent initial equilibration in an isothermal-isobaric (NPT) ensemble at a temperature of 298 K and an elevated pressure of 1 kBar. This high-pressure equilibration was conducted over a duration of 20 ns to ensure sufficient compaction and mixing of the PDDA and ATP molecules. Subsequently, the system pressure was reduced to 1 bar while maintaining the temperature at 298 K. This secondary equilibration phase was also carried out for 20 ns, allowing the system to adjust to the lower pressure and achieve a stable state. The equilibrated cubic box was then expanded along the z-axis by a factor of 5, resulting in a slab configuration with dimensions $L_x = L_y = 9.5$ nm and $L_z = 50$ nm. This expansion introduced a vacuum surrounding the slab in the z-direction. To model a realistic solvent environment, the vacuum was filled with MARTINI 2.0 water beads and counterions corresponding to the PDDA and ATP molecules present in the slab. We added 25536 solvent beads and 2500 Na^+ and 2500 Cl^- ions for this purpose, which corresponds to 920 mM ionic concentration. We also replaced 2553 solvent beads with antifreeze beads as per protocol for using MARTINI2.0 water[71]. The solvated slab system was then equilibrated in an anisotropic NPT ensemble, maintaining the pressure at 1 bar along the z-axis ($P_z = 1$ bar) and keeping the slab incompressible in the x and y directions. This equilibration phase was performed for 5 ns, ensuring that the solvent far from the slab reached bulk density at the corresponding ionic strength. Following equilibration, production simulations were conducted for 3.5 μs in the NVT ensemble with a trajectory saving frequency of 1 ns. The slab was then transferred to a deionized water environment, following the same protocol used during the initial cubic box simulation. The system was equilibrated again in an anisotropic NPT ensemble to attain the bulk water density appropriate for the new ionic conditions, in a box with dimensions 9.5 nm × 9.5 nm × 52.66 nm. This was followed by a production simulation for 3.5 μs in the NVT ensemble, with data collected at 1 ns intervals. To ensure statistical robustness, three independent starting configurations were generated and subjected to the same simulation protocol. For all simulations, the last 1.5 μs of the data were used for analysis to ensure equilibrium conditions and exclude transient effects. All simulation parameters employed in the slab configuration are consistent with those utilized in our cubic box simulations.

Simulation details

All randomly dispersed systems were energy minimized using the steepest descent algorithm prior to equilibration of the system for 100 ns in NPT ensemble where the temperature was maintained constant at 298 K with the Berendsen thermostat[73] with 1 ps time constant and pressure was maintained constant at 1 bar using Berendsen barostat[73] with a time constant of 3 ps. Following the NPT equilibration, a production run of 7 μs was carried out in the NPT ensemble with the same parameters with a trajectory saving

frequency of 1 ns. A timestep of 20 fs was implemented for integrating Newton's equation of motion using the leapfrog algorithm[74]. The run parameters were adapted from Vogele et al.[65] A cutoff distance of 1.2 nm was used both for the van der Waals interactions and short-range Coulombic interactions. Long-range electrostatic interaction was managed by implementing the Particle Mesh Ewald (PME) method[75]. All simulations have been performed by using the GROMACS 2021.4[76–78] software package. For visualization of molecular trajectories VMD 1.9.4[79] software has been used. For analyzing the trajectories, we have used MDAnalysis 2.2.0[80,81] and the OVITO program[82].

Cluster analysis

To quantify the coacervate formation during our simulations, we employed a clustering algorithm based on a minimum distance criterion as in one of our recent works[83]. Here, we considered any ATP or PDDA in the same cluster if the minimum distance (r_{cut}) between any PDDA or ATP beads is less than or equal to 0.85 nm. We built an adjacency matrix based on this criterion and then identified the clusters based on the connected components. Further information on the clustering algorithm can be found in this work[83]. We then measured the time evolution of the fraction of PDDA and ATP molecules ($f_{cluster}$) within the largest cluster for both supernatant and DI water systems for all simulation replicas, as depicted in Supplementary Figs. 18 and 19 respectively. Result for one representative simulation is presented in Fig. 1C. When $f_{cluster}$ was found to reach and remain at 1.0 without any deviation, we considered the cluster to be well-formed and stable; and referred to that cluster as the coacervate.

For all the independent simulations corresponding to the supernatant system, we ensemble averaged the individual samples over the period of the last 3.5 μs (from 3.5 μs to 7 μs), whereas for DI water independent simulations, the ensemble averaging time slab was considered from 0 μs to 3.5 μs.

Asphericity index

We also calculated the time evolution of the asphericity index (A_S) of the largest cluster formed in both "supernatant" and "DI water" systems to examine the shape of the clusters. This asphericity index (A_S) was calculated following the expression[84]:

$$A_S = \frac{1}{2} \left(\sum_{i > j = 1}^{3} \left(R_i^2 - R_j^2 \right)^2 \right) \Big/ \left(\sum_{i=1}^{3} \left(R_i^2 \right)^2 \right) \quad (1)$$

where R_i^2 are the principal radii of gyration of the cluster represented by all of its PDDA and ATP beads. A_S changes between 0 and 1, where $A_S = 0$ for a perfectly spherical object and $A_S = 1$ for a rodlike object.

Ion residence time correlation function $C_{res}^{ion}(t)$

To understand the quantitative differences between ions residing in different regions of the coacervates, namely the "core" and "surface", we calculated the lifetimes of ions residing in those regions. This residence time was calculated from residence time correlation function $C_{res}^{ion}(t)$ via the following equation[85,86]:

$$C_{res}^{ion}(\Delta t) = \frac{\langle h(t') H(\Delta t; t') \rangle}{\langle h \rangle} \quad (2)$$

where h(t') takes a value of 1 when a particle is residing in the targeted region at time t' and 0 when it is not. $H(\Delta t; t')$ takes a value of 1 if the particle is continuously residing in that region ("core" for residence time of core ions or "surface" for residence time of surface ions) for the timespan of Δt starting from time t'; $H(\Delta t; t')$ equates to 0 if the particle goes out of the region at any given point of time within time t' to $t' + \Delta t$. That is:

$$H(\Delta t; t') = \prod_{t = t'}^{t' + \Delta t} h(t). \quad (3)$$

and $< h >$ denotes ensemble averaged $h(t')$.

To be able to calculate the timescales associated with these correlation decays, namely residence timescales, we fit these time correlation functions using multi-exponential fit-functions as follows:

$$C_{res}^{ion}(\Delta t) = \sum_{x=1}^{n} a_i \exp\left(-\frac{\Delta t}{\tau_i} \right), \quad (4)$$

where τ_i are the relaxation (residence) time scales, a_i are prefactors, and the index i runs over 2 or 3 depending on whether the bi-exponential or tri-exponential function represents data better.

In this analysis, we need an explicit description of the 'core' and 'surface' of the coacervate (as well as the rest of the simulation box, which is referred to as 'bulk'). Upon visual inspection of the coacervates (e.g., snapshots in Supplementary Figs. 5 and 6), we observed that their shapes tend to deviate from a sphere, posing a challenge in accurately defining the surface region of the clusters. To define the surface region, we developed the following prescription:

(1) The coacervate was projected on three mutually perpendicular principal planes defined by the three (dynamic) principal axes of the cluster (see Fig. 1D).

(2) Subsequently, these projections on three mutually perpendicular planes were plotted together on a single graph using distinct colors, and the common rectangular area of overlapping projections was identified and marked.

(3) We observed that the common rectangular area encloses between sets of two horizontal (at $y = -2$ nm, $y = 2$ nm) and two vertical red lines (at $x = -2$ nm, $x = 2$ nm). We then considered the overlapping volume in three dimensions as a sphere of radius ($r_{inner} = 2.8$ nm), i.e., half diagonal of this rectangular area. We consider this volume as the "core" (see Fig. 1D).

(4) Finally, the area between the inner radius ($r_{inner} = 2.8$ nm) and outer radius ($r_{outer} = 5$ nm) was considered as the interfacial region. It should be noted that $r_{out} = 5$ nm is extracted from the density profile plot of PDDA and ATP beads mentioned in Fig. 2A in the main text, where 5 nm was found to be the maximum radial distance from the center where PDDA or ATP beads were found. We employed this protocol for defining the "core" and "surface" regions for all eight sample simulations.

We presented the projections with this prescription in Supplementary Fig. 20 for all independent simulations in the supernatant. By analyzing these projections, we developed the following for defining the "core", "surface", and "bulk" regions: (1) core region: the spherical region of radius $r_{inner} = 2.8$ nm centered at the center of mass (COM) of the coacervate, (2) surface region: the spherical shell within radii $r_{inner} = 2.8$ nm and $r_{outer} = 5$ nm, (3) bulk region: region outside the radial distance $r_{outer} = 5$ nm from the COM of the coacervates.

Data availability

All data generated or analyzed during this study are included in this published article (and its Supplementary Information files). Coarse-grained descriptions of PDDA and ATP molecule; a snapshot of coacervate before transferring it to DI water; and radial distribution function for PDDA-Cl beads with Martini 2.0 force field, sigmoidal fits for mass density profiles of PDDA and ATP, the time evolution of the fraction of clustering beads in coacervates, asphericity index, ratio of positive to negative ions within coacervates, displacement of tagged ions after transferring the coacervate to DI water, and residence time correlation function for all eight replica simulations with random starting configurations are presented in Supplementary Figures. Results associated with hypothetical Charge Exchange simulations also presented in Supplementary Figures. Tables containing multi-exponential fit parameters of residence time correlation functions for associated "core" and "surface" ions in the supernatant and DI water are presented in Supplementary Tables. Supplementary Movie of the

coacervation process, transferring the coacervate to DI water along with extended simulation in DI water is also included.

References

1. Bungenberg de Jong, H. & Kruyt, H. Coacervation (partial miscibility in colloid systems). *Proc. K. Ned. Akad. Wet* **32**, 849–856 (1929).
2. Wagner, R. Some comments and questions äbout the germinal vesicular germinativa. *Müllers Arch. Anat. Physiol. Sci. Med.* **268**, 373–377 (1835).
3. Valentin, G. *Repertorium für anatomie und physiologie* (Veit, 1837).
4. Schwann, T. & Hünseler, F. *Microscopic Investigations ön the Correspondence in the Structure and Growth of Animals and Plants* 176 (W. Engelmann, 1910).
5. Frankel, E. A., Bevilacqua, P. C. & Keating, C. D. Polyamine/nucleotide coacervates provide strong compartmentalization of mg2+, nucleotides, and RNA. *Langmuir* **32**, 2041–2049 (2016).
6. Drobot, B. et al. Compartmentalised RNA catalysis in membrane-free coacervate protocells. *Nat. Commun.* **9**, 3643 (2018).
7. Aumiller Jr, W. M., Davis, B. W. & Keating, C. D. Phase separation as a possible means of nuclear compartmentalization. *Int. Rev. Cell Mol. Biol.* **307**, 109–149 (2014).
8. Brangwynne, C. P. et al. Germline p granules are liquid droplets that localize by controlled dissolution/condensation. *Science* **324**, 1729–1732 (2009).
9. Gall, J. G. The centennial of the cajal body. *Nat. Rev. Mol. Cell Biol.* **4**, 975–980 (2003).
10. Späth, F. et al. Molecular design of chemically fueled peptide–polyelectrolyte coacervate-based assemblies. *J. Am. Chem. Soc.* **143**, 4782–4789 (2021).
11. Gomes, E. & Shorter, J. The molecular language of membraneless organelles. *J. Biol. Chem.* **294**, 7115–7127 (2019).
12. Banani, S. F., Lee, H. O., Hyman, A. A. & Rosen, M. K. Biomolecular condensates: organizers of cellular biochemistry. *Nat. Rev. Mol. Cell Biol.* **18**, 285–298 (2017).
13. Jia, T. Z. & Fraccia, T. P. Liquid crystal peptide/DNA coacervates in the context of prebiotic molecular evolution. *Crystals* **10**, 964 (2020).
14. Mason, A. F., Buddingh', B. C., Williams, D. S. & Van Hest, J. C. Hierarchical self-assembly of a copolymer-stabilized coacervate protocell. *J. Am. Chem. Soc.* **139**, 17309–17312 (2017).
15. Schmitt, C. & Turgeon, S. L. Protein/polysaccharide complexes and coacervates in food systems. *Adv. Colloid Interface Sci.* **167**, 63–70 (2011).
16. Veis, A. & Aranyi, C. Phase separation in polyelectrolyte systems. I. Complex coacervates of gelatin. *J. Phys. Chem.* **64**, 1203–1210 (1960).
17. Stewart, R. J., Wang, C. S. & Shao, H. Complex coacervates as a foundation for synthetic underwater adhesives. *Adv. Colloid Interface Sci.* **167**, 85–93 (2011).
18. Kaur, S., Weerasekare, G. M. & Stewart, R. J. Multiphase adhesive coacervates inspired by the sandcastle worm. *ACS Appl. Mater. Interfaces* **3**, 941–944 (2011).
19. Zhao, Q. et al. Underwater contact adhesion and microarchitecture in polyelectrolyte complexes actuated by solvent exchange. *Nat. Mater.* **15**, 407–412 (2016).
20. Rodriguez, A. M. B., Binks, B. P. & Sekine, T. Emulsion stabilisation by complexes of oppositely charged synthetic polyelectrolytes. *Soft Matter* **14**, 239–254 (2018).
21. Bago Rodriguez, A. M., Binks, B. P. & Sekine, T. Emulsions stabilized with polyelectrolyte complexes prepared from a mixture of a weak and a strong polyelectrolyte. *Langmuir* **35**, 6693–6707 (2019).
22. Ma, L., Fang, X. & Wang, C. Peptide-based coacervates in therapeutic applications. *Front. Bioeng. Biotechnol.* **10**, 1100365 (2023).
23. Agrawal, A., Douglas, J. F., Tirrell, M. & Karim, A. Manipulation of coacervate droplets with an electric field. *Proc. Natl. Acad. Sci. USA* **119**, e2203483119 (2022).
24. Alberti, S., Gladfelter, A. & Mittag, T. Considerations and challenges in studying liquid-liquid phase separation and biomolecular condensates. *Cell* **176**, 419–434 (2019).
25. Priftis, D., Laugel, N. & Tirrell, M. Thermodynamic characterization of polypeptide complex coacervation. *Langmuir* **28**, 15947–15957 (2012).
26. Spruijt, E., Westphal, A. H., Borst, J. W., Cohen Stuart, M. A. & van der Gucht, J. Binodal compositions of polyelectrolyte complexes. *Macromolecules* **43**, 6476–6484 (2010).
27. Priftis, D., Farina, R. & Tirrell, M. Interfacial energy of polypeptide complex coacervates measured via capillary adhesion. *Langmuir* **28**, 8721–8729 (2012).
28. Chollakup, R., Beck, J. B., Dirnberger, K., Tirrell, M. & Eisenbach, C. D. Polyelectrolyte molecular weight and salt effects on the phase behavior and coacervation of aqueous solutions of poly (acrylic acid) sodium salt and poly (allylamine) hydrochloride. *Macromolecules* **46**, 2376–2390 (2013).
29. Jha, P. K., Desai, P. S., Li, J. & Larson, R. G. pH and salt effects on the associative phase separation of oppositely charged polyelectrolytes. *Polymers* **6**, 1414–1436 (2014).
30. Qin, J. et al. Interfacial tension of polyelectrolyte complex coacervate phases. *ACS Macro Lett.* **3**, 565–568 (2014).
31. Priftis, D. & Tirrell, M. Phase behaviour and complex coacervation of aqueous polypeptide solutions. *Soft Matter* **8**, 9396–9405 (2012).
32. Rumyantsev, A. M., Jackson, N. E. & De Pablo, J. J. Polyelectrolyte complex coacervates: recent developments and new frontiers. *Annu. Rev. Condens. Matter Phys.* **12**, 155–176 (2021).
33. Smokers, I. B., van Haren, M. H., Lu, T. & Spruijt, E. Complex coacervation and compartmentalized conversion of prebiotically relevant metabolites. *ChemSystemsChem* **4**, e202200004 (2022).
34. Lindhoud, S., de Vries, R., Norde, W. & Stuart, M. A. C. Structure and stability of complex coacervate core micelles with lysozyme. *Biomacromolecules* **8**, 2219–2227 (2007).
35. van der Kooij, H. M. et al. On the stability and morphology of complex coacervate core micelles: from spherical to wormlike micelles. *Langmuir* **28**, 14180–14191 (2012).
36. Overbeek, J. T. & Voorn, M. J. Phase separation in polyelectrolyte solutions. Theory of complex coacervation. *J. Cell. Comp. Physiol.* **49**, 7–26 (1957).
37. Borue, V. Y. & Erukhimovich, I. Y. A statistical theory of weakly charged polyelectrolytes: fluctuations, equation of state and microphase separation. *Macromolecules* **21**, 3240–3249 (1988).
38. Castelnovo, M. & Joanny, J. Phase diagram of diblock polyampholyte solutions. *Macromolecules* **35**, 4531–4538 (2002).
39. Kudlay, A., Ermoshkin, A. V. & Olvera de La Cruz, M. Complexation of oppositely charged polyelectrolytes: effect of ion pair formation. *Macromolecules* **37**, 9231–9241 (2004).
40. Mahdi, K. A. & Olvera de La Cruz, M. Phase diagrams of salt-free polyelectrolyte semidilute solutions. *Macromolecules* **33**, 7649–7654 (2000).
41. Perry, S. L. & Sing, C. E. Prism-based theory of complex coacervation: excluded volume versus chain correlation. *Macromolecules* **48**, 5040–5053 (2015).
42. Lytle, T. K. & Sing, C. E. Transfer matrix theory of polymer complex coacervation. *Soft Matter* **13**, 7001–7012 (2017).
43. Danielsen, S. P., Panyukov, S. & Rubinstein, M. Ion pairing and the structure of gel coacervates. *Macromolecules* **53**, 9420–9442 (2020).
44. Sing, C. E. & Qin, J. Bridging field theory and ion pairing in the modeling of polyelectrolytes and complex coacervation. *Macromolecules* **56**, 5941–5963 (2023).
45. Jeon, J. & Dobrynin, A. V. Monte Carlo simulations of polyampholyte-polyelectrolyte complexes: effect of charge sequence and strength of electrostatic interactions. *Phys. Rev. E* **67**, 061803 (2003).

46. Orkoulas, G., Kumar, S. K. & Panagiotopoulos, A. Z. Monte Carlo study of coulombic criticality in polyelectrolytes. *Phys. Rev. Lett.* **90**, 048303 (2003).

47. Ou, Z. & Muthukumar, M. Entropy and enthalpy of polyelectrolyte complexation: Langevin dynamics simulations. *J. Chem. Phys.* **124**, 154902 (2006).

48. Lee, J., Popov, Y. O. & Fredrickson, G. H. Complex coacervation: a field theoretic simulation study of polyelectrolyte complexation. *J. Chem. Phys.* **128**, 224908 (2008).

49. Riggleman, R. A., Kumar, R. & Fredrickson, G. H. Investigation of the interfacial tension of complex coacervates using field-theoretic simulations. *J. Chem. Phys.* **136**, 024903 (2012).

50. Audus, D. J. et al. Phase behavior of electrostatically complexed polyelectrolyte gels using an embedded fluctuation model. *Soft Matter* **11**, 1214–1225 (2015).

51. Williams, D. S. et al. Polymer/nucleotide droplets as bio-inspired functional micro-compartments. *Soft Matter* **8**, 6004–6014 (2012).

52. Lu, T., Nakashima, K. K. & Spruijt, E. Temperature-responsive peptide–nucleotide coacervates. *J. Phys. Chem. B* **125**, 3080–3091 (2021).

53. Muhoza, B. et al. Combined plant protein modification and complex coacervation as a sustainable strategy to produce coacervates encapsulating bioactives. *Food Hydrocoll.* **124**, 107239 (2022).

54. Andreev, M., Prabhu, V. M., Douglas, J. F., Tirrell, M. & de Pablo, J. J. Complex coacervation in polyelectrolytes from a coarse-grained model. *Macromolecules* **51**, 6717–6723 (2018).

55. Chen, S. & Wang, Z.-G. Driving force and pathway in polyelectrolyte complex coacervation. *Proc. Natl. Acad. Sci. USA* **119**, e2209975119 (2022).

56. Neitzel, A. E. et al. Polyelectrolyte complex coacervation across a broad range of charge densities. *Macromolecules* **54**, 6878–6890 (2021).

57. Bobbili, S. V. & Milner, S. T. A simple simulation model for complex coacervates. *Soft Matter* **17**, 9181–9188 (2021).

58. Yu, B., Liang, H., Rumyantsev, A. M. & de Pablo, J. J. Isotropic-to-nematic transition in salt-free polyelectrolyte coacervates from coarse-grained simulations. *Macromolecules* **55**, 9627–9639 (2022).

59. Chang, L.-W. et al. Sequence and entropy-based control of complex coacervates. *Nat. Commun.* **8**, 1273 (2017).

60. Benayad, Z., von Bülow, S., Stelzl, L. S. & Hummer, G. Simulation of fus protein condensates with an adapted coarse-grained model. *J. Chem. Theory Comput.* **17**, 525–537 (2020).

61. Ingólfsson, H. I. et al. Multiscale simulations reveal tdp-43 molecular-level interactions driving condensation. *Biophys. J.* **122**, 4370–4381 (2023).

62. Tsanai, M. et al. Coacervate formation studied by explicit solvent coarse-grain molecular dynamics with the martini model. *Chem. Sci.* **12**, 8521–8530 (2021).

63. Liu, Y., Wang, X., Wan, Z., Ngai, T. & Tse, Y.-L. S. Capturing coacervate formation and protein partition by molecular dynamics simulation. *Chem. Sci.* **14**, 1168–1175 (2023).

64. Souza, P. C. et al. Martini 3: a general purpose force field for coarse-grained molecular dynamics. *Nat. Methods* **18**, 382–388 (2021).

65. Vögele, M., Holm, C. & Smiatek, J. Coarse-grained simulations of polyelectrolyte complexes: martini models for poly (styrene sulfonate) and poly (diallyldimethylammonium). *J. Chem. Phys.* **143**, 243151 (2015).

66. Schroer, C. F. et al. Charge-dependent interactions of monomeric and filamentous actin with lipid bilayers. *Proc. Natl. Acad. Sci. USA* **117**, 5861–5872 (2020).

67. Li, L. et al. Phase behavior and salt partitioning in polyelectrolyte complex coacervates. *Macromolecules* **51**, 2988–2995 (2018).

68. Zhang, P., Shen, K., Alsaifi, N. M. & Wang, Z.-G. Salt partitioning in complex coacervation of symmetric polyelectrolytes. *Macromolecules* **51**, 5586–5593 (2018).

69. Agrawal, A. et al. Did the exposure of coacervate droplets to rain make them the first stable protocells? *Sci. Adv.* **10**, eadn9657 (2024).

70. Press, C. *Handbook of Biochemistry and Molecular Biology* (CRC Press, 2010).

71. Marrink, S. J., Risselada, H. J., Yefimov, S., Tieleman, D. P. & De Vries, A. H. The martini force field: coarse grained model for biomolecular simulations. *J. Phys. Chem. B* **111**, 7812–7824 (2007).

72. Yesylevskyy, S. O., Schäfer, L. V., Sengupta, D. & Marrink, S. J. Polarizable water model for the coarse-grained martini force field. *PLoS Comput. Biol.* **6**, e1000810 (2010).

73. Berendsen, H. J., Postma, J. V., Van Gunsteren, W. F., DiNola, A. & Haak, J. R. Molecular dynamics with coupling to an external bath. *J. Chem. Phys.* **81**, 3684–3690 (1984).

74. Birdsall, C. K. & Langdon, A. B. *Plasma Physics via Computer Simulation* (CRC Press, 2004).

75. Essmann, U. et al. A smooth particle mesh Ewald method. *J. Chem. Phys.* **103**, 8577–8593 (1995).

76. Bekker, H. et al. Gromacs-a parallel computer for molecular-dynamics simulations. In *4th International Conference on Computational Physics (PC 92)*, 252–256 (World Scientific Publishing, 1993).

77. Páll, S., Abraham, M. J., Kutzner, C., Hess, B. & Lindahl, E. Tackling exascale software challenges in molecular dynamics simulations with gromacs. In *Solving Software Challenges for Exascale: International Conference on Exascale Applications and Software, EASC 2014, Stockholm, Sweden, April 2-3, 2014, Revised Selected Papers 2*, 3–27 (Springer, 2015).

78. Abraham, M. J. et al. Gromacs: high performance molecular simulations through multi-level parallelism from laptops to supercomputers. *SoftwareX* **1**, 19–25 (2015).

79. Humphrey, W., Dalke, A. & Schulten, K. VMD—visual molecular dynamics. *J. Mol. Graph.* **14**, 33–38 (1996).

80. Michaud-Agrawal, N., Denning, E. J., Woolf, T. B. & Beckstein, O. Mdanalysis: a toolkit for the analysis of molecular dynamics simulations. *J. Comput. Chem.* **32**, 2319–2327 (2011).

81. Gowers, R. J. et al. Mdanalysis: a python package for the rapid analysis of molecular dynamics simulations. In *Proceedings of the 15th Python in Science Conference*, Vol. 98, 105 (SciPy, 2016).

82. Stukowski, A. Visualization and analysis of atomistic simulation data with OVITO—the open visualization tool. *Model. Simul. Mater. Sci. Eng.* **18**, 015012 (2009).

83. Zerze, G. H. Optimizing the martini 3 force field reveals the effects of the intricate balance between protein–water interaction strength and salt concentration on biomolecular condensate formation. *J. Chem. Theory Comput.* **20**, 1646–1655 (2023).

84. Van Giessen, A. & Szleifer, I. Monte Carlo simulations of chain molecules in confined environments. *J. Chem. Phys.* **102**, 9069–9076 (1995).

85. Luzar, A. & Chandler, D. Hydrogen-bond kinetics in liquid water. *Nature* **379**, 55–57 (1996).

86. Chandra, A. Effects of ion atmosphere on hydrogen-bond dynamics in aqueous electrolyte solutions. *Phys. Rev. Lett.* **85**, 768 (2000).

Acknowledgements

Author contributions

G.H.Z. designed research; A.B. performed research; G.H.Z. and H.Z. supervised the research; H.Z. contributed new reagents/analytic tools; A.B.,

Competing interests

The authors declare no competing interests.

Additional information

Supplementary information The online version contains supplementary material available at https://doi.org/10.1038/s42004-024-01304-1.

Correspondence and requests for materials should be addressed to Gül H. Zerze.

Peer review information *Communications Chemistry* thanks Zhen-Gang Wang and the other, anonymous, reviewers for their contribution to the peer review of this work.

Reprints and permissions information is available at http://www.nature.com/reprints

Publisher's note Springer Nature remains neutral with regard to jurisdictional claims in published maps and institutional affiliations.